Proceedings of the
International Conference on Mechanical Engineering and Renewable Energy 2011
(ICMERE2011) 22- 24 December 2011, Chittagong, Bangladesh

ICMERE2011-PI-106

COMPUTATIONAL STUDY OF TURBULENT FLOW OVER A SPHERE

Md. Taibur Rahman [1], Md. Kamrul Hasan[2]

[1] Department of Mechanical and Production Engineering, AUST, Dhaka-1208, Bangladesh.
[2]Department of Mechanical Engineering, CUET, Chittagong-4349, Bangladesh.
Email address: [1]khushbu.cuet@gmail.com, [2]shimulcuet@gmail.com

Abstract*- A computational investigation is made to study the effect of velocity and diameter of the sphere on the pressure co-efficient, skin friction co-efficient and velocity vectors of the turbulent flow over sphere at different flow regimes. Deviation of negative pressure co-efficient from positive pressure co-efficient is smaller for higher velocity in pressure recovery region. The slope of the pressure co-efficient curve is higher for higher diameter of sphere. Pressure co-efficient is higher negative for larger diameter of sphere. Skin friction co-efficient increases with the increase of diameter and velocity of fluid.*

Keywords: Control volume, pressure, velocity, contour, turbulent flow, pressure co-efficient, skin friction, velocity vector, flow regime.

1. INTRODUCTION

Applications of computational fluid dynamics (CFD) to the maritime industry continue to grow as this advanced technology takes advantage of the increasing speed of computers. In the last two decades, different areas of incompressible flow modeling including grid generation techniques, solution algorithms and turbulence modeling, and computer hardware capabilities have witnessed tremendous development. In view of these developments, computational fluid dynamics (CFD) can offer a cost-effective solution to many problems in underwater bodies. However, effective utilization of CFD for marine hydrodynamics depends on proper selection of turbulence model, grid generation and boundary resolution.

Turbulence modeling is still a necessity as even with the emergence of high performance computing since analysis of complex flows by direct numerical simulations (DNS) is untenable. The peer approach, the large-Eddy simulation (LES), still remains expensive. Hence, simulation of underwater hydrodynamics continues to be based on the solution of the Reynolds-averaged Navier-Stokes (RANS) equations. Various researchers used turbulence modeling to simulate flow around axisymmetric bodies since late seventies. Patel and Chen [1] made an extensive review of the simulation of flow past axisymmeric bodies. Choi and Chen [2] gave calculation method for the solution of RANS equation, together with k-ε turbulence model. Sarkar et al. [3] used a low-Re k-ε model of Lam and Bremhorst [4] for simulation of flow past underwater bodies.

A considerable amount of research work has been published on flow over a sphere. The basic structure of the flow past a sphere has been experimentally investigated using a variety of approaches, including flow visualization by Achenbach [5], Taneda [6], Bakic [7] etc. Recent time-accurate computations of laminar and turbulent flow around spheres using different methods are reported by many researchers, among them the work of Gregory [8], Kalro [9] and Sun and Chwang [10] are remarkable. In this present study, Spalart-Allmaras (S-A) and shear stress transport (SST) k-ω turbulence models are used to simulate fully turbulent flow over underwater sphere.

2. THEORETICAL FORMULATION

CFD is based on the fundamental governing equations of fluid dynamics. The Equations are continuity, momentum, and energy equations. These equations speak physics. They are the mathematical statements of three fundamental physical principles upon which all of fluid dynamics is based:

1. Mass is conserved.
2. Newton's second law, F = ma.
3. Energy is conserved.

2.1 Conservation laws

If we restrict our attention to single-phase fluids, the law of mass conservation expresses the fact that mass cannot be created in such a fluid system, nor can disappear from it.

At a point on the control surface, the flow velocity is $\vec{v}$, the unit normal vector is $\vec{n}$ and dS denotes an-elemental surface area. For the time rate of change of the total mass inside the finite volume Ω**.** The conserved

quantity in this case is the density ρ, surface area ($\vec{v} * \vec{n}$), by convection $\vec{n}$ always points out of the control volume, we speak of Inflow if the product ($\vec{v} * \vec{n}$) is negative, and of outflow if it is positive and hence the mass flow leaves the control volume. There are no volume or surface sources present.

Hence integral form of the continuity equation - the conservation law of mass can be represent as:

$$\frac{\partial}{\partial t}\int_{\Omega} \rho d\,\Omega + \oint_{\partial\Omega}\rho(\vec{v} * \vec{n})\,dS = 0 \qquad (2.1)$$

The momentum equation by recalling the particular form of Newton's second law which states that the variation of momentum is caused by the net force acting on an mass element. For the momentum of an infinitesimally small portion of the control volume Ω we have- $\rho\vec{v}d\Omega$ which is the variation in time of momentum. The convective flux tensor $-\oint_{\partial\Omega}\rho\vec{v}(\vec{v} * \vec{n})dS$, which describes the transfer of momentum across the boundary of the control volume, consists in the Cartesian coordinate system of the following three components-

X-component: $pu\vec{v}$,
Y-component: $pv\vec{v}$,
Z-component: $pw\vec{v}$.

The diffusive flux is zero, since there is no diffusion of momentum possible for a fluid at rest. We can identify two kinds of forces acting on the control volume:

1. External volume or body forces, which act directly on the mass of the volume.
2. Surface forces, which act directly on the surface of the control volume.

Considering all of these the momentum equation can be represent as :

$$\frac{\partial}{\partial t}\int_{\Omega} \rho\vec{v}d\,\Omega + \oint_{\partial\Omega}\rho\vec{v}(\vec{v}\,.\,\vec{n})\,dS = \int_{\Omega} \rho\vec{f_e}\,d\Omega - \oint_{\partial\Omega}p\,\vec{n}\mathrm{dS} + \oint_{\partial\Omega}(\bar{\bar{\tau}}\,.\,\vec{n})\,\mathrm{dS} \qquad (2.2)$$

Equation 2.2 is called the momentum equation. Where, body force per unit volume, denoted as- $\rho\vec{f}_e$, viscous stress tensor as $\bar{\bar{\tau}}$. Here, momentum conservation inside an arbitrary control volume R which is fixed in space.

The energy equation can be represent as-

$$\frac{\partial}{\partial t}\int_{\Omega} \rho E d\Omega + \oint_{\partial\Omega}\rho H(\vec{v}\,.\,\vec{n})\,dS = \int_{\partial\Omega}\kappa(\nabla T\,.\,\vec{n})dS + \int_{\Omega}(\rho\vec{f_e}\,.\,\vec{v} + \dot{q_h}) - \oint_{\partial\Omega}p\,(\vec{v}\,.\,\vec{n}\,)\mathrm{dS} + \oint_{\partial\Omega}(\bar{\bar{\tau}}\,.\,\vec{v})\,.\vec{n}\mathrm{dS} \qquad (2.3)$$

Here, we will denote the heat sources - the time rate of heat transfer per unit mass - as $\vec{q}_h$. Together with the rate of work done by the body forces $\vec{f}_e$, total energy E, temperature gradient ∇T .

3. STANDARD K - EPSILON TURBULENCE MODEL

At high Reynolds numbers [11] the rate of dissipation of kinetic energy ϵ is equal to the viscosity multiplied by the fluctuating vorticity. An exact transport equation for the fluctuating vorticity, and thus the dissipation rate, can be derived from the Navier Stokes equation. The k - epsilon model consists of the turbulent kinetic energy equation-

$$\frac{\partial k}{\partial t} + \mathrm{div}\,(\rho\underline{u}k) = \mathrm{div}\left(\left[\mu_{\mathrm{tam}} + \frac{\rho v_t}{\sigma_k}\right]\mathrm{grad}k\right) + \sigma v_t G - \rho\varepsilon \qquad (3.1)$$

And the dissipation rate (ε) equation-

$$\frac{\partial \varepsilon}{\partial t} + \mathrm{div}\,(\rho\underline{u}\varepsilon) = \mathrm{div}\left(\left[\mu_{\mathrm{tam}} + \frac{\rho v_t}{\sigma_\varepsilon}\right]\mathrm{grad}\varepsilon\right) + C_{1\varepsilon}\rho v_t \mathrm{G}\frac{\varepsilon}{k} - C_{2\varepsilon}\rho\frac{\varepsilon^2}{k} \qquad (3.2)$$

Where *G* represents the turbulent generation rate – G=2

$$\left(\left[\frac{\partial u}{\partial x}\right]^2 + \left[\frac{\partial v}{\partial y}\right]^2 + \left[\frac{\partial w}{\partial z}\right]^2\right) + \left(\frac{\partial u}{\partial y} + \frac{\partial v}{\partial x}\right)^2 + \left(\frac{\partial u}{\partial z} + \frac{\partial w}{\partial x}\right)^2 + \left(\frac{\partial w}{\partial y} + \frac{\partial v}{\partial z}\right)^2 \qquad (3.3)$$

Model constants are-

$C_{1\varepsilon} = 1.44$, $C_{2\varepsilon} = 1.92$, $C_{\mu} = 0.09$, $\sigma_k = 1.0$, $\sigma_\varepsilon = 1.3$

4. BOUNDARY CONDITIONS

The bottom and top boundary of the domain is modeled as an axis boundary. Additionally, the left boundary of the domain are modeled as 'velocity inlet', the right boundary is modeled as an 'outflow boundary', and the surface of the body itself is modeled as a 'wall'.

5. METHODOLOGY

Grid construction, the computational domain for sphere model is divided into two regions: the boundary layer region and the free stream region. Dividing the domain in this fashion is a common practice in problems where the effects of the viscous boundary layer that forms on the body are expected to significantly affect the flow field and where enhanced grid resolution in the vicinity of the boundary layer is important. The boundary layers are attached to the spheres and the direction of the boundary layer grids is defined such that the grids extended into the interior of the domains. Based on prior experience with numerical simulations involving boundary layers and the expected growth of the boundary layer meridionally along the sphere, both boundary layer meshes are approximately 3 cm in height. Increasing the number of rows in the boundary layer meshes only served to vary cell density, and did not change the total height of the mesh. Finally, the growth factors are chosen to increase the resolution of the meshes at the base of the boundary layers (where flow parameter gradients are largest) while still maintaining high grid resolution, low cell skewness at the top of the boundary layers, and a total boundary layer mesh thickness of approximately 3 cm. Low skewness is important to ensure similar cell proportions between outer boundary layer cells and neighboring free stream region cells. The boundary layer grid parameters for the sphere models are shown in Table .1 If the growth factor is not listed in the following tables, it would be considered as unity.

Table 1: Boundary layer parameters of sphere grids.

Meridional node count on sphere	First row thickness in boundary layer	Boundary layer growth factor	Number of rows in boundary layer
120	0.0001	1.24	20

Table 2. The node spacing of sphere on the edges of the domains for each edge node distribution.

Node on FS 1	Growth factor on FS 1	Node on FS 2
50	0.9	12

FS = Front section;

Table 3. The node spacing of sphere on the edges of the domains for each edge node distribution.

Node on RS 1	Growth factor on RS 1	Node on RS 2	Growth factor on RS 2	Node count on TB
50	1.111	12	20	40

RS = Rear section; TB = Top boundary;

Table 4: Sphere boundary node spacing distributions.

Front face		Middle face	
No. of Nodes	Growth factor	No. of Nodes	Growth factor(both direction)
45	1.04	80	1.02

Table 5: Sphere boundary node spacing distributions.

Rear face		Normal to the axis	
No. of Nodes	Growth factor	No. of Nodes	Growth factor
75	1.05	90	1.05

Grid construction, the computational domain is divided into three faces: Middle face, Front face and Rear face. At first, the edges of the faces are meshed, and then, using the edge meshes, the interiors of the faces are meshed. The node spacing on the edges of the domain for each node distribution is given in the Table 4 and Table 5. Once the edges are meshed, the interior of the domains need to be meshed using automatic face mesh generation scheme. The meshing scheme that is chosen is pave meshing scheme. The tri-pave scheme creates an unstructured grid of mesh elements, which is particularly desirable for its applicability to a wide range of face geometries, its ability to deal with irregularly shaped interiors, and its ease of use. There is no restriction on mesh node spacing imposed by the pave scheme since only triangular face elements are used. More cells are constructed near the surface of the sphere to tackle the high velocity gradient in the boundary layer region of the viscous flow. Fig.1 shows the grid for the sphere, which is symmetric about the axis of rotation. A commercial software GAMBIT is used for grid generation.

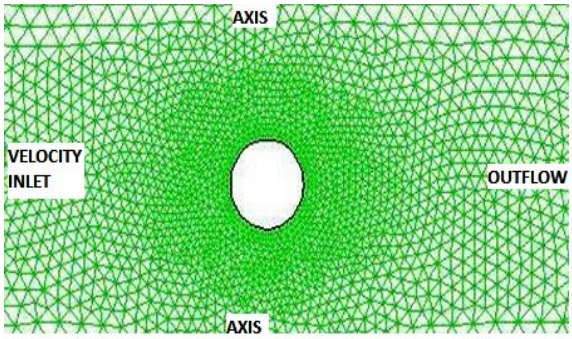

Fig.1: Sphere grid with boundary conditions.

In Fig-1,the bottom and top boundary of the domain is modeled as an axis boundary. Additionally, the left boundary of the domain are modeled as 'velocity inlet', the right boundary is modeled as an 'outflow boundary', and the surface of the body itself is modeled as a 'wall'.

6. RESULTS AND DISCUSSION

Figure-1 shows the grid that I've generated to carried out computational study. The size of the grid is 60*20*30 in r, □, □ direction respectively. There are 6874 cells, 10436 faces, 3562 nodes, one partition in the grid and tri-pave mesh system is used for the grid generation.
Here we have carried out two types of simulation. One effect of diameter change over a sphere when velocity is fixed. Another one effect of velocity change on a fixed diameter.

Figure-2 shows the velocity vector for a diameter of 4cm and Re no-1.09533e6 .It shows the characteristics features like stagnation region, flow separation point and the recirculation region. It is seen that separation occurs at an angle of 1.5769 radian. Here different color and size of arrow shows the magnitude of velocity vector. At the point of forward stagnation point and after the flow past the sphere velocity is less than other place which is shown by blue color. Red color shows the maximum velocity magnitude and yellow for medium velocity magnitude.

We have seen the effect of diameter change for four different diameters.For a diameter of 6cm and Re no1.64300e6.It is seen that separation occurs at angle of 1.5069 radian for a diameter of 8cm and Re no-2.19068e6. Here separation occurs at angle of 1.1817 radian, for a diameter of 10cm and Re no-2.73834e6. Here separation occurs at angle of 1.1325 radian. To see how separation occurs for a fixed diameter and varying velocity we have seen the effect for four different velocity.

We have also seen the effect of velocity change for a fixed diameters For a diameter of 4cm, v=6 m/s and Re no-1.64300e6, separation occurs at angle of 1.5700 radian for v=6 m/s, for a diameter of 4cm, v=8 m/s and Re no-2.19067e6. Here Separation occurs at angle of 1.5048 radian ,for a diameter of 4cm, v=10 m/s and Re

no-2.73834e6.It is seen that separation occurs at an angle of 1.2021 radian, for a diameter 4cm, v=12m/s and Re no-3.28601e6. It is seen that separation occurs at an angle of 1.1269 radian .

Figure-3 shows the separation point of the sphere. For different velocity and different diameter of sphere separation point will vary.

Figure-4 shows that the distribution of pressure coefficients for different diameters on different positions of the sphere. The pressure co-efficient is positive at the stagnation point and decreases with the increase of angular position from the forward stagnation point. Near the stagnation region the slope of the curves are higher for larger diameters of the sphere that means the flow separation occurs earlier in case of larger diameter of the sphere.

Figure-5 shows the distribution of pressure co-efficient on different position of the sphere for different velocities. At the stagnation point pressure is positive in all cases, with the increase of velocity, the magnitude of maximum pressure (Negative) decreases. At the stagnation point the pressure is higher (Negative) for lower velocity that means in the pressure recovery region the pressure recovers at a higher rate for higher velocity.

From figure-6 it is seen that skin friction co-efficient increases with the increase of angular position from the forward stagnation point for different diameter of sphere and at a fixed velocity of 4 m/s. After the separation point skin friction co-efficient decreases. At the rear stagnation point shin friction coefficient is lower. At the inflection point skin friction co-efficient is higher.

From figure-7 it is seen that skin friction co-efficient increases with the increase of angular position from the forward stagnation point for different velocity and on a sphere diameter of 4cm and at a fixed velocity of 4 m/s. After the separation point skin friction co-efficient decreases. At the rear stagnation point shin friction coefficient is lower. At the inflection point skin friction co-efficient is higher.

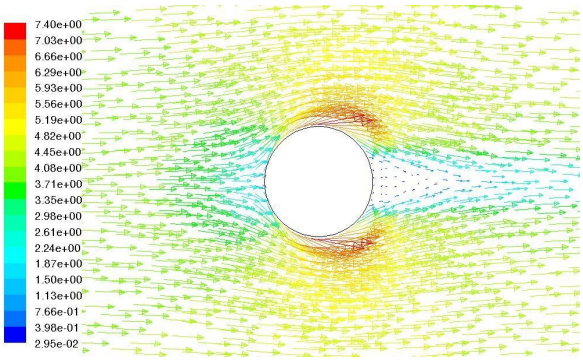

Fig-2: Velocity magnitude for a diameter of 4cm and Re no-1.09533e6.

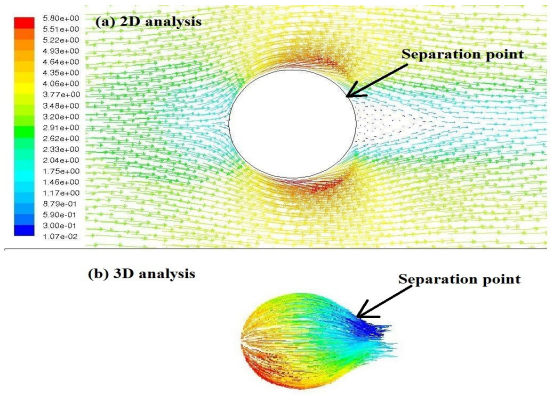

Fig. 3 Velocity vector showing the separation point.

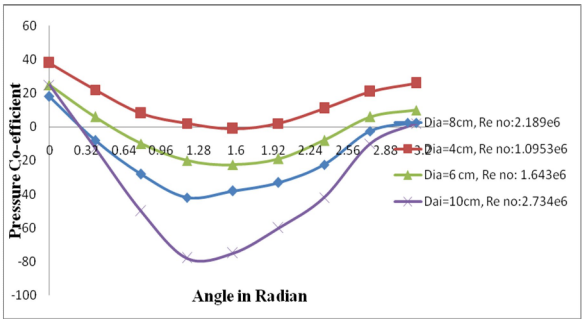

Fig-4: Pressure Co-efficient Vs Angle in radian fo different diameter and v=4m/s.

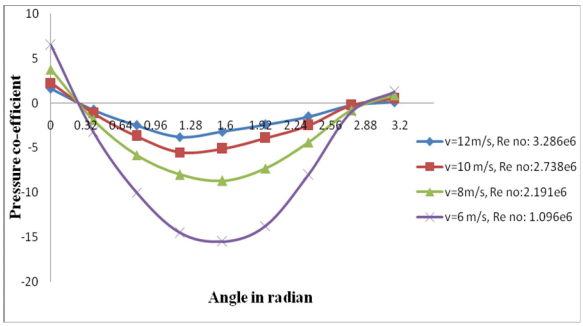

Fig-5: Pressure Co-efficient Vs Angle in radian for different velocity and d=4cm.

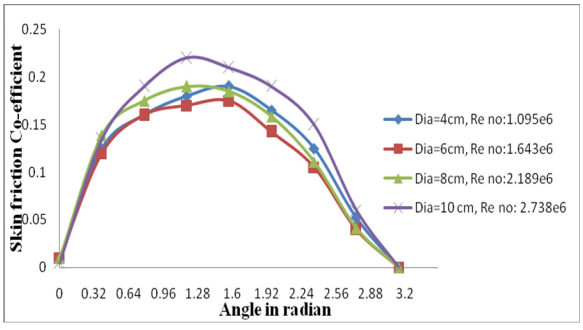

Fig-6: Skin Co-efficient Vs Angle in radian for different diameter and v=4m/s.

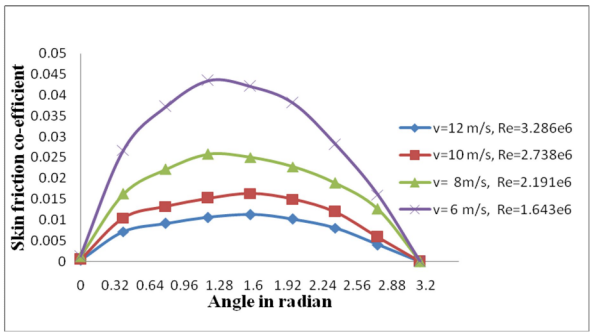

Fig-7: Skin Co-efficient Vs Angle in radian for different velocity and d=4cm.

7. CONCLUSION

The flow around a sphere in infinite flow has the characteristic tendency of flow separation along with coanda effect making the flow adhere to the surface and delaying the flow separation. The adverse pressure gradient and coanda effect depend upon the magnitude of turbulence intensity and magnitude of approach velocity. For fully developed turbulent velocity profile at approach, the flow adheres to the sphere due to the coanda effect. These features have significant influence on skin friction and pressure distribution.

The optimum performance of fluid machinery, such as fans, turbines, pumps, compressors etc. can only be predicted with accurate understanding of flow of separation. By experimental study we have to face lots of problem to find separation point. Computational Fluid Mechanics has become popular to find separation point as well as any simulation of Fluid Mechanics.

8. REFERENCES

[1] V. C. Patel and H. C. Chen, Journal of Ship Research **30** (3), 202 (1986).

[2] S. K. Choi and C. J. Chen, Laminar and turbulent flows past two dimensional and axisymmetric bodies, Iowa Institute of Hydraulic Research, IIHR Report 334-II (1990).

[3] T. Sarkar, P. G. Sayer, and S. M. Fraser, International Journal for Numerical Methods in Fluids 25, 1301 (1997). doi:10.1002/(SICI)1097-0363(19971215)25:11<1301::AID-FLD612>3.0.CO;2-G

[4] C. K. G. Lam and K. Bremhorst, ASME Journal Fluid Engineering 103, 456 (1981

[5] E. Achenbach, Journal of Fluid Mechanics, 54 (3), 565 (1972). doi:10.1017/S0022112072000874

[6] S. Taneda, Journal of Fluid Mechanics, 85, 187 (1978). doi:10.1017/S0022112078000580

[7] V. Bakic, Ph.D. Thesis, TUHH Hamburg, Germany, 2002

[8] J.S. Gregory, Master's Thesis, Dept. of Air Force, Air Force Institute of Technology, Ohio, 2000.

[9] V. Kalro and T. Tezduyan, Computer Methods in Applied Mechanics and Engineering, l (151), 267 (1998).

[10] R. Sun, and T. A. Chwang, Structural Control Health Monitoring, l (13), 147 (2006).

[11] http://www.cfd-online.com/Wiki/standard k-epsilon model.

[12] H. K. Versteeg and W. Malalasekera, An Introduction to Computational Fluid Dynamics-The Finite Volume Method (Longman Scientific and Technical, U.K., 1995).

[13] T. Cebeci, J. R. Shao, F. Kafyeke, E. Laurendeau, Computational Fluid Dynamics for Engineers (Horizons Publishing Inc., Long Beach, California, 2005).